Electronic Supplementary Material (ESI) for Environmental Science: Nano.

Supporting Information for:

Montmorillonite helps BiOCl photodegradation of antibiotics

Gang Wang[a], *Shilin Zhang*[a, c], *Hongxiu Lu*[a], *Chang Lu*[b], *Mei Yang*[a], *Kai Tang*[a], *Aidong Tang*[a, c, *]

[a] College of Chemistry and Chemical Engineering, Central South University, Changsha, Changsha 410083, China.

[b] College of Minerals Processing and Bioengineering, Central South University, Changsha 410083, China.

[c] Engineering Research Center of Nano-Geomaterials of Ministry of Education, Laboratory of Advanced Mineral Materials, and Faculty of Materials Science and Chemistry, China University of Geosciences, Wuhan 430074, China

* Corresponding author. Tel: +86-731-8887 9616; E-mail address: adtang@csu.edu.cn (A. Tang).

Supplementary Texts:

Text S1. Materials and reagents

The raw montmorillonite particles (K-10), L-ascorbic acid (LAA) and tetracycline hydrochloride (TCH) were purchased from Aladdin Reagent Co. Ltd. Sodium chloride (NaCl), ethylenediaminetetraacetic acid disodium salt (EDTA-2Na), concentrated hydrochloric acid (HCl, 36%~38%), sodium hydroxide (NaOH), sodium nitrate ($NaNO_3$), sodium sulfate (Na_2SO_4), and sodium carbonate (Na_2CO_3) were provided by Sinopharm Group Co. Ltd. Perfluorinated resin (Nafion), bismuth nitrate pentahydrate ($Bi(NO_3)_3 \cdot 5H_2O$), ethylene glycol (EG), and isopropanol (IPA) were supplied by Macklin Reagent Co. Ltd. All reagents were of analytical grade and used without further purification. The water from the Xiangjiang River was collected from the Changsha section in Hunan, while the water from the Yudai River was obtained from the campus of Central South University. Unless otherwise specified, deionized (DI) water was used throughout the entire experimental process.

Text S2. Radical capture experiments

In order to investigate the degradation mechanism of TCH, a radical capture experiment was designed to identify the dominant active species. The specific procedure was similar to the photocatalytic activity assessment experiment, except that

the corresponding scavengers were added before turning on the light. Specifically, this study used LAA, EDTA-2Na and IPA as the scavengers for superoxide radicals ($\bullet O_2^-$), photogenerated holes (h^+) and hydroxyl radicals (•OH), respectively. In all active species capture experiments, the concentration of scavengers was 1 mM.

Text S3. Photoelectrochemical measurements

All photoelectrochemical measurements were performed by an electrochemical workstation (Ivium V54813 electrochemical analyzer) using a standard three-electrode system. A platinum sheet was used as counter electrode and Ag/AgCl (KCl 3M) as reference electrode. The photocatalyst was coated on ITO conductive glass (coated area of 1 cm^2) as the working electrode. The electrolyte was 0.5 M Na_2SO_4 solution, and the oxygen in the solution was removed using N_2 before measurement. The instantaneous photocurrent (I-t) curves were measured under 1.0 V bias potential, 60 s on/off chopper illumination with a distance of approximately 3 cm between the Xenon light source and the working electrode. The Mott-Schottky (M-S) plot was obtained at a frequency of 500, 1000 and 2000Hz. Electrochemical impedance spectroscopy (EIS) was measured over a frequency range of 0.01 Hz to 1 MHz with a current-voltage amplitude of 0.01 V.

Text S4. Characterization

X-ray diffractometer (XRD, Bruker D8 advance) with a Cu Kα radiation source (λ = 0.15418 nm) and a scanning angle range of 5 to 80° was used to analyze the structures

and crystal phases of all samples. Fourier transform infrared spectroscopy (FTIR; IR-960, Japan) with a scanning range from 4000 to 400 cm^{-1} was used to gather functional group information. Transmission electron microscopy (TEM, FEI TF20) and scanning electron microscope (SEM, Zeiss Sigma300) were used to analyze the morphology of all samples. The specific surface areas were measured according to Brunauer-Emmett-Teller (BET) method at 77 K using a nitrogen adsorption apparatus (ASAP 2020 Plus, Micromeritics, America) and the pore size distributions were measured by the Barrett-Joyner-Halenda (BJH) method applying the desorption branch of the isotherm. Thermo Scientific K-Alpha spectrometer with a monochromatic Al-Kα X-ray source was utilized to gather X-ray photoelectron spectroscopy (XPS) data to examine the chemical composition and valence states, and the reference C 1s peak at 284.8 eV was used to calibrate the binding energy. Using $BaSO_4$ as a reference, the UV-vis diffuse reflectance spectra (UV-vis-DRS) of photocatalyst were examined on UV-2550 (Shimadzu). The Fluorescence spectrometer (Hitachi F-7000) was employed to acquire the photoluminescence (PL) spectra, with an excitation wavelength of 325 nm. Total organic carbon (TOC) was determined by using a total organic analyzer (TOC-L, Shimadzu) with 680 ℃ combustion catalytic oxidation method. Electron spin resonance (ESR) spectroscopy (Bruker EMX PLUS) for detection of reactive radicals. Intermediate products generated during the degradation of TC were monitored using liquid chromatography-mass spectrometry (LC-MS, Agilent 1260/6460), with the mobile phase consisting of acetonitrile/water (80/20, v/v), a flow rate of 0.4 mL min^{-1}, and an injection volume of 10 μL.

Supplementary Tables:

Table S1. Specific amounts of $Bi(NO_3)_3 \cdot 5H_2O$ and Mt in different composites.

Samples \ Materials	$Bi(NO_3)_3 \cdot 5H_2O$ (mg)	Mt (mg)
BiOCl	485	0
3B/1M	485	86.7
2B/1M	485	130
1B/1M	485	260
1B/2M	485	520
1B/3M	485	780

Table S2. Textural properties of as-prepared composites.

Samples	BET surface area (m^2/g)	Pore volume (cm^3/g)	average pore diameter (nm)
BiOCl	21.96	0.131	23.89
3B/1M	71.78	0.183	10.19
2B/1M	89.54	0.194	8.67
1B/1M	126.38	0.234	7.41
1B/2M	170.29	0.296	6.95
1B/3M	185.65	0.299	6.44
Mt	240.42	0.361	6.01

Table S3. Percentages of each element for BiOCl.

Element	Weight %	Atomic %
O	8.98	43.76
Cl	12.21	26.84
Bi	78.81	29.40

Table S4. Percentages of each element for Mt.

Element	Weight %	Atomic %
O	55.99	69.37
Mg	1.60	1.30
Al	7.40	5.44
Si	32.66	23.05
Fe	2.35	0.84

Table S5. Percentages of each element for 1B/1M.

Element	Weight %	Atomic %
O	37.13	55.48
Al	17.69	15.68
Si	30.62	26.07
Bi	12.58	1.44
Cl	1.97	1.33

Table S6. Comparison of the degradation performance of different BiOCl-based photocatalysts for TCH.

Photocatalyst	Testing conditions	D (mg)	C_{TCH}	Degradation Rate	Ref.
SCF/BiOCl	500 W Xenon lamp	100	100 mL 20 mg/L	60% (40 min)	[1]
BiOCl@CeO_2	300 W Xenon lamp ($\lambda \geq 420$ nm)	50	100 mL 10 mg/L	92% (120 min)	[2]
C NFs/BiOCl	300 W Xenon lamp ($\lambda \geq 420$ nm)	50	100 mL 10 mg/L	50% (60 min)	[3]
$BiOCl_{0.2}Br_{0.8}$	300 W Xenon lamp	20	100 mL 50 mg/L	75% (60 min)	[4]
Ta_3N_5/BiOCl	300 W Xenon lamp ($\lambda \geq 400$ nm)	30	100 mL 20 mg/L	89.6% (60 min)	[5]
BiOCl/CdS	300 W Xenon lamp	10	15 mL 10 mg/L	75% (100 min)	[6]
Bi_4O_7/Cu-BiOCl	1000 W Xenon lamp ($\lambda \geq 420$ nm)	30	50 mL 30 mg/L	91% (60 min)	[7]
BiOCl/TiO_2	300 W Xenon lamp ($\lambda \geq 420$ nm)	50	100 mL 20 mg/L	84% (150 min)	[8]
Ag/AgCl/BiOCl	500 W Xenon lamp ($\lambda \geq 420$ nm)	30	80 mL 20 mg/L	83% (60 min)	[9]
Fe_3O_4/BiOCl/BiOI	300 W Xenon lamp	40	50 mL 40 mg/L	89% (80 min)	[10]
BiOCl/ Montmorillonite	300 W Xenon lamp	20	100 mL 20 mg/L	95.9% (60 min)	This work

Supplementary Figures:

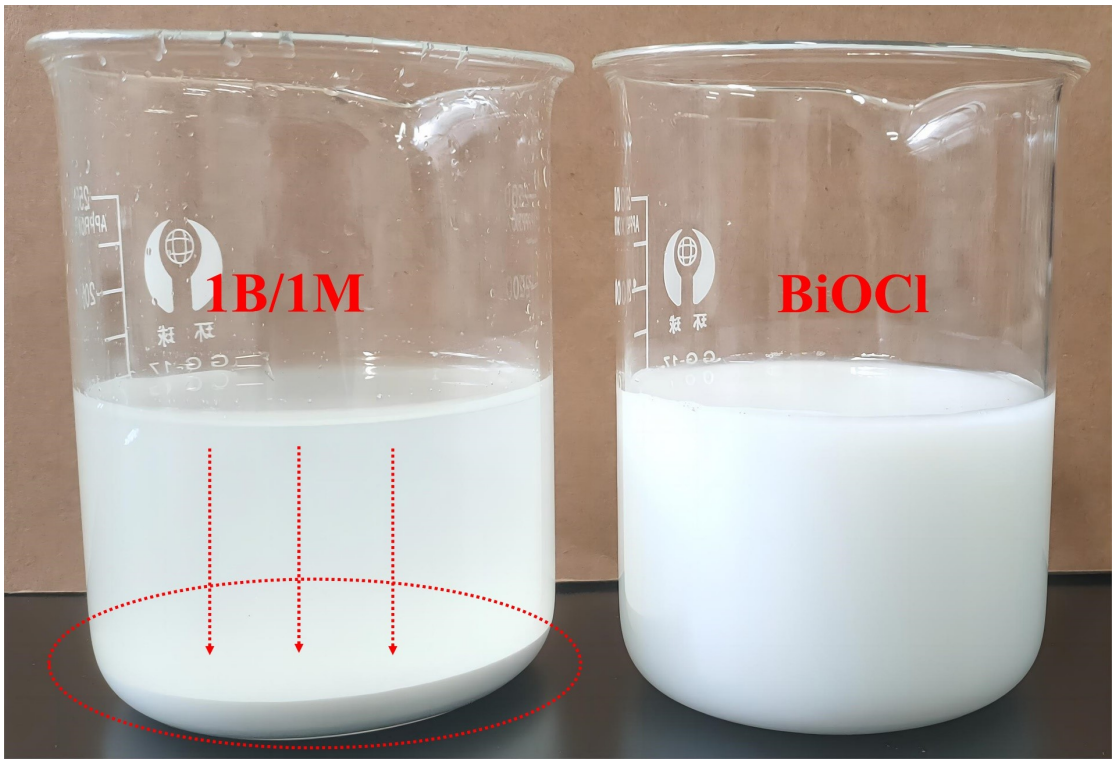

Fig. S1. Photographs of 1B/1M and BiOCl after one hour of resting

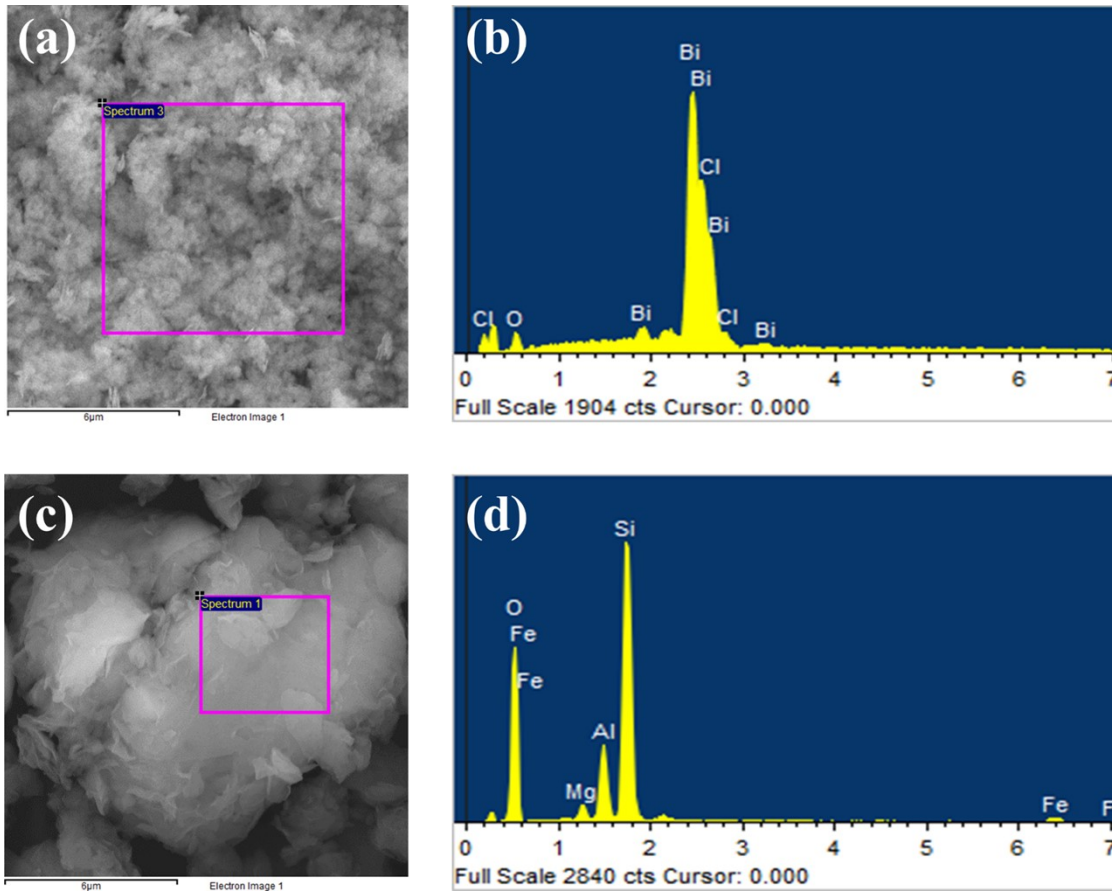

Fig. S2. EDX spectra for (a, b) BiOCl and (c, d) Mt

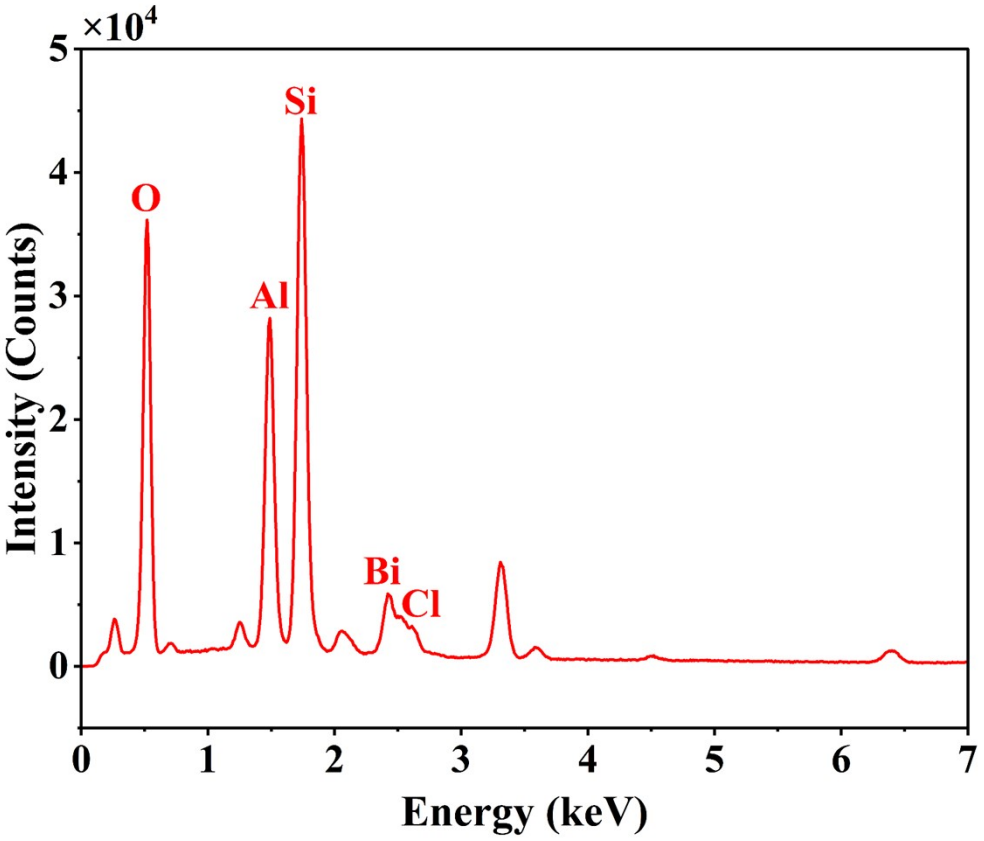

Fig. S3. EDX spectra for 1B/1M.

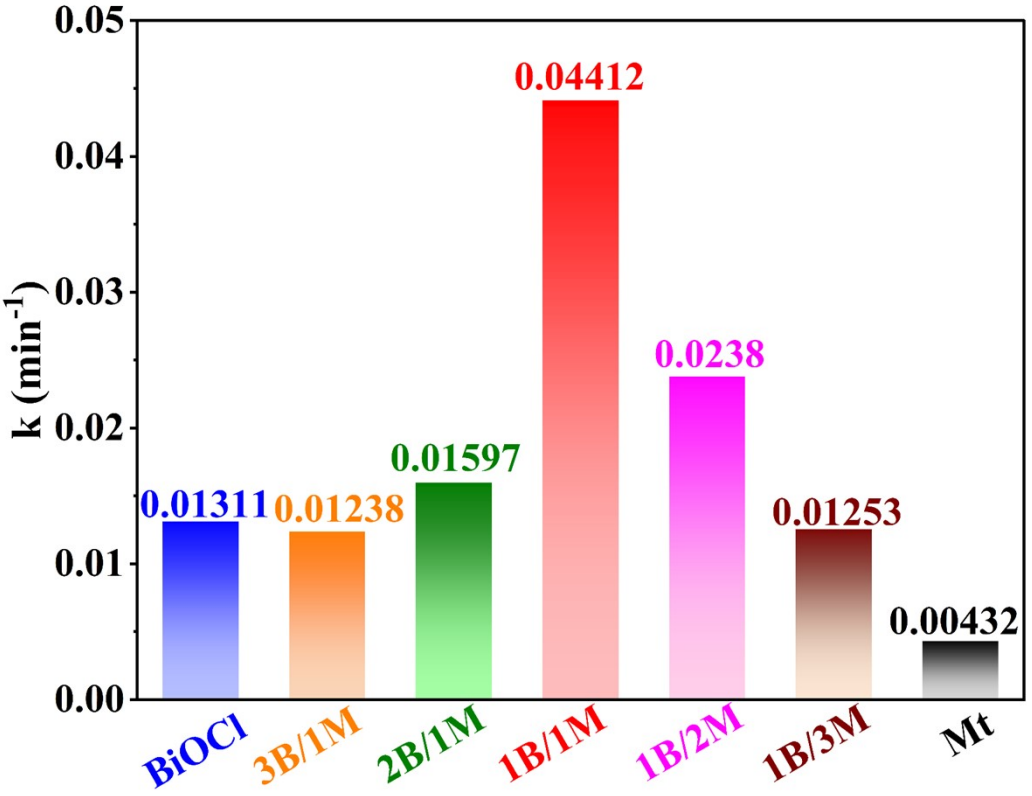

Fig. S4. Kinetic k values for the photocatalytic degradation of TCH by different photocatalysts.

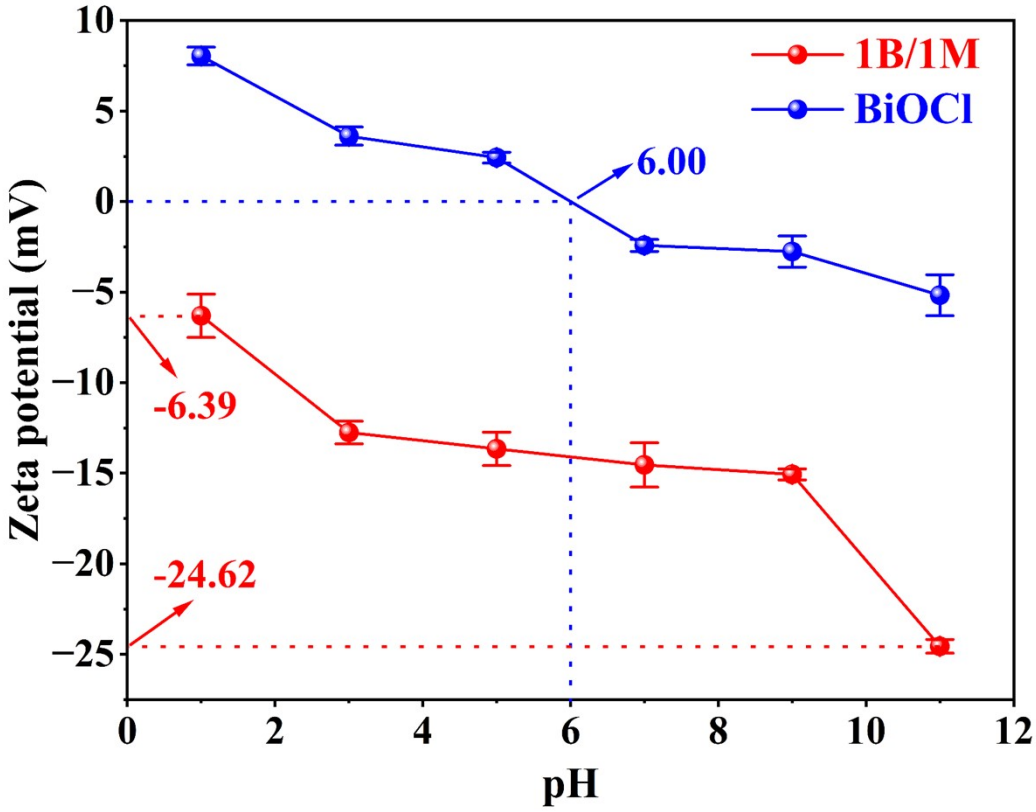

Fig. S5. Zeta potential of BiOCl and 1B/1M as a function of pH.

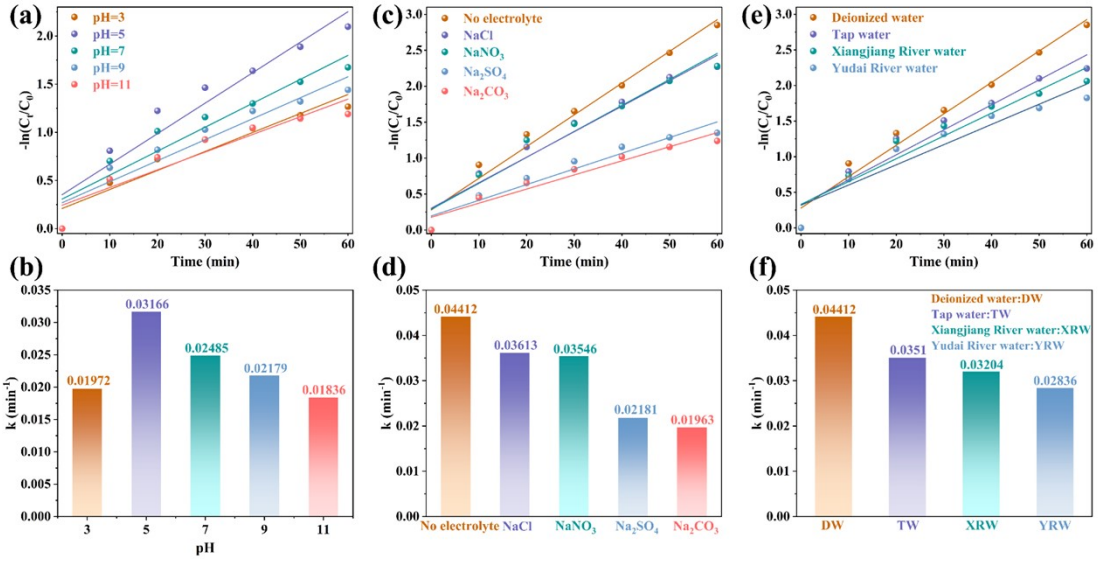

Fig. S6. Kinetic information of the reaction under different external factors: (a) pH, (b) inorganic ions, and (c) different water qualities.

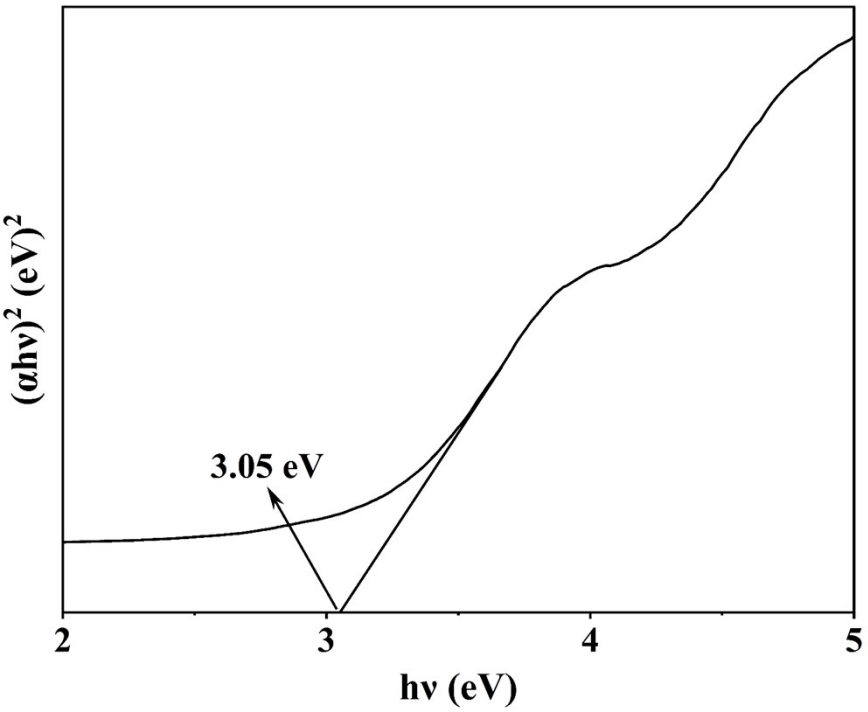

Fig. S7. Tauc plots of Mt.

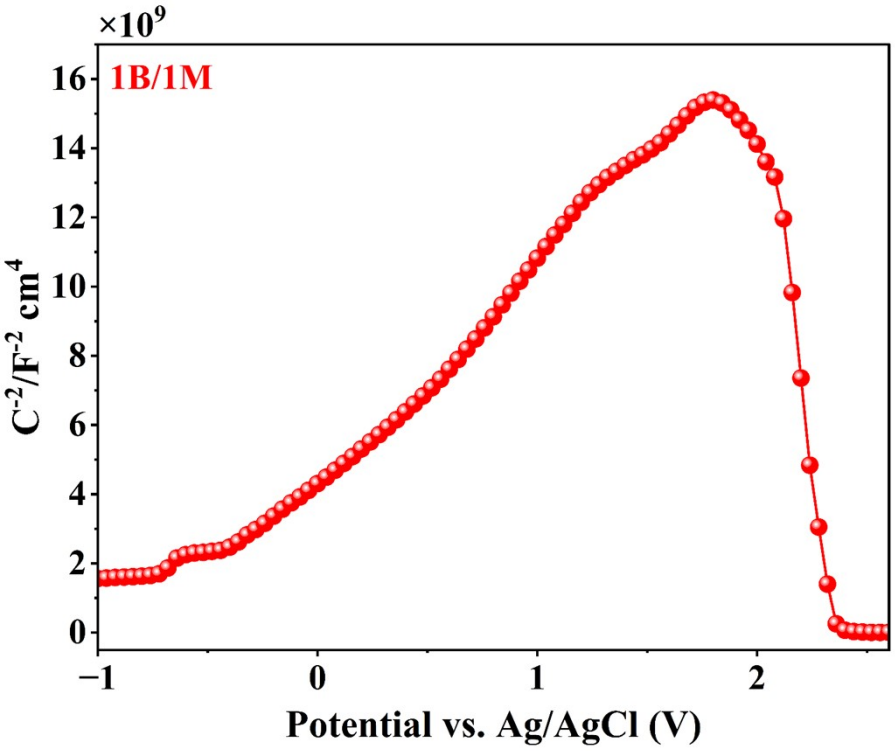

Fig. S8. M−S plots of 1B/1M.

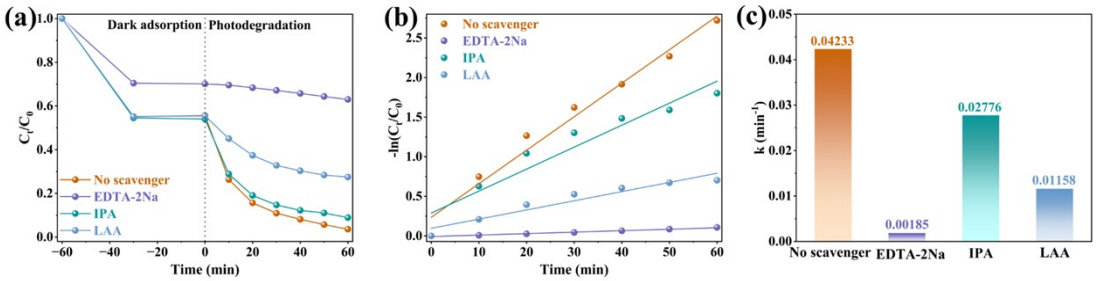

Fig. S9. Kinetic information corresponding to the addition of different scavengers.

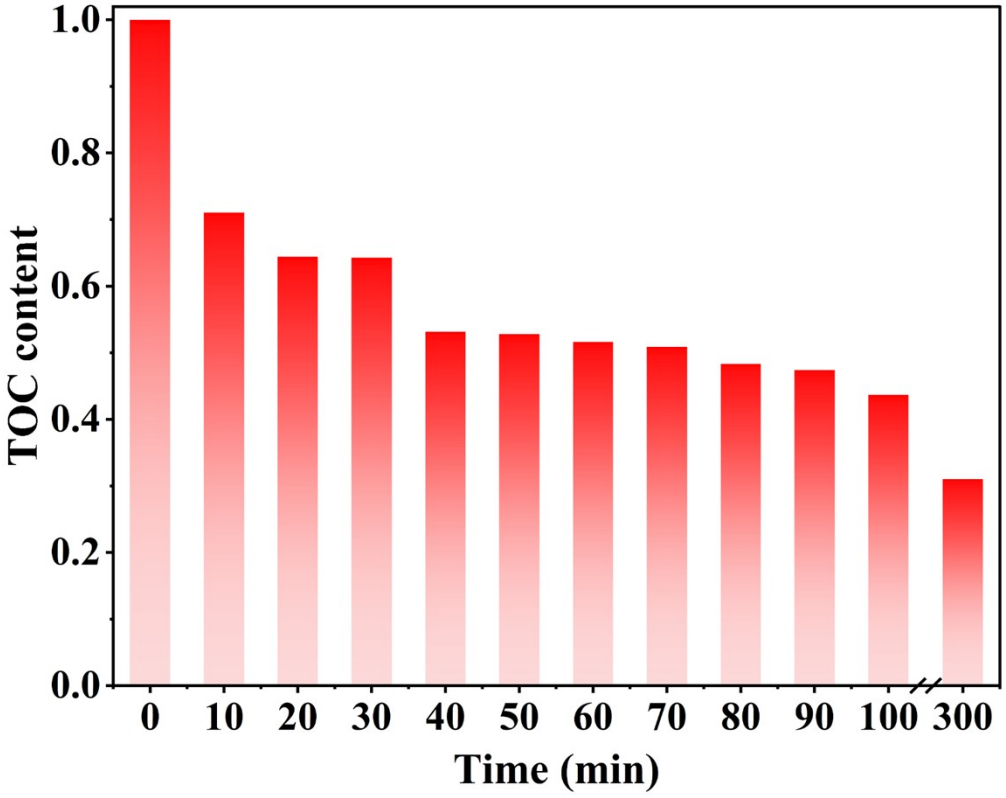

Fig. S10. Variation of TOC content in the system with degradation time.

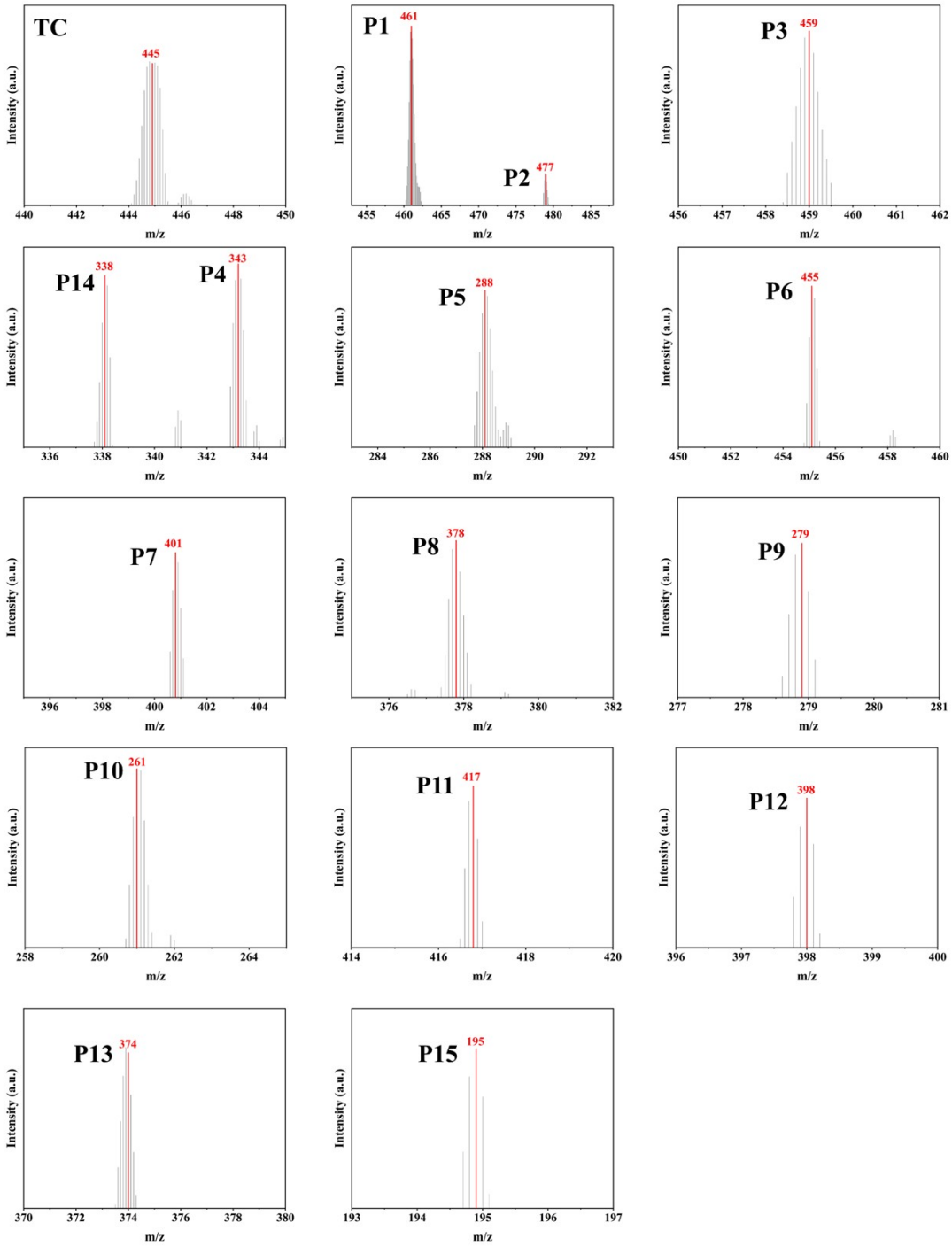

Fig. S11. Mass spectrometry of TC intermediates.

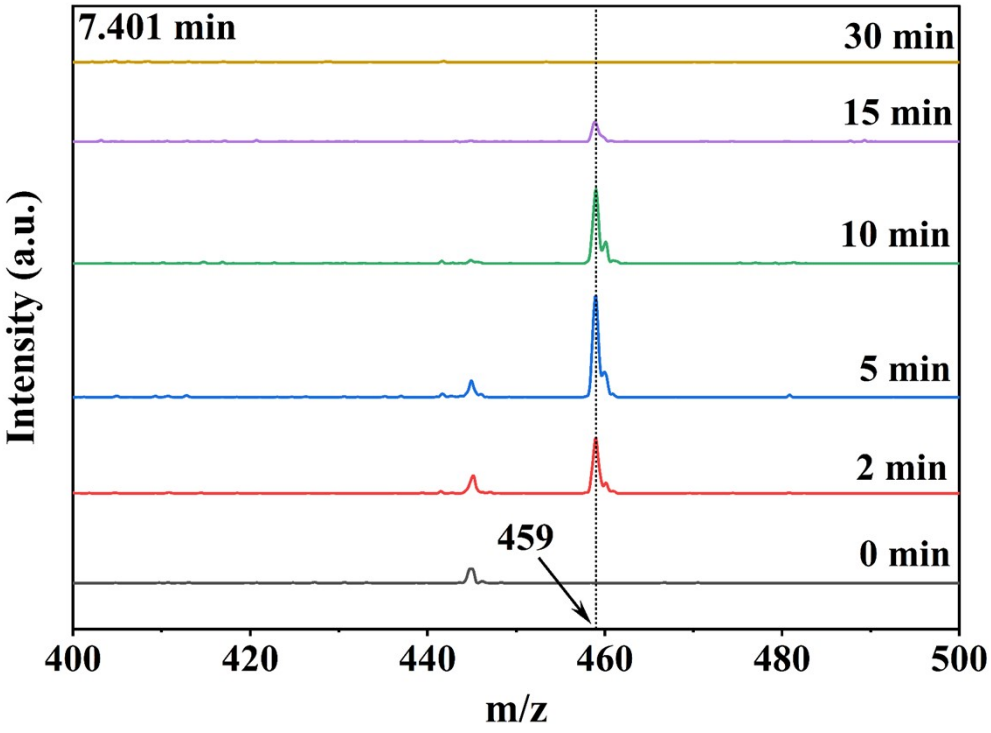

Fig. S12. Concentration changes of P3 intermediates during degradation.

As the entire preparation process of the 1B/1M was conducted in an open container at room temperature, we predicted that a large amount of product could be obtained by simply scaling up the precursor proportion. To verify this idea, we scaled up the precursor proportion by five and ten times, respectively (Fig. S13), and obtained the corresponding products, whose quality was roughly proportional to the precursor proportion (Fig. S14).

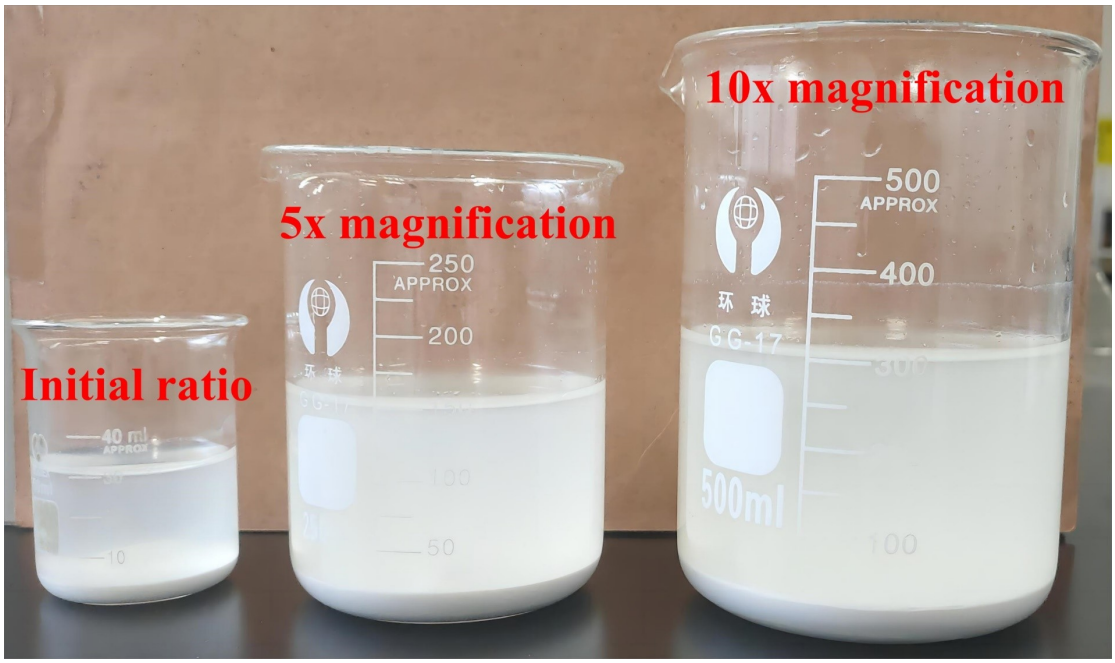

Fig. S13. Digital photo of preparing 1B/1M by scaling up the precursor.

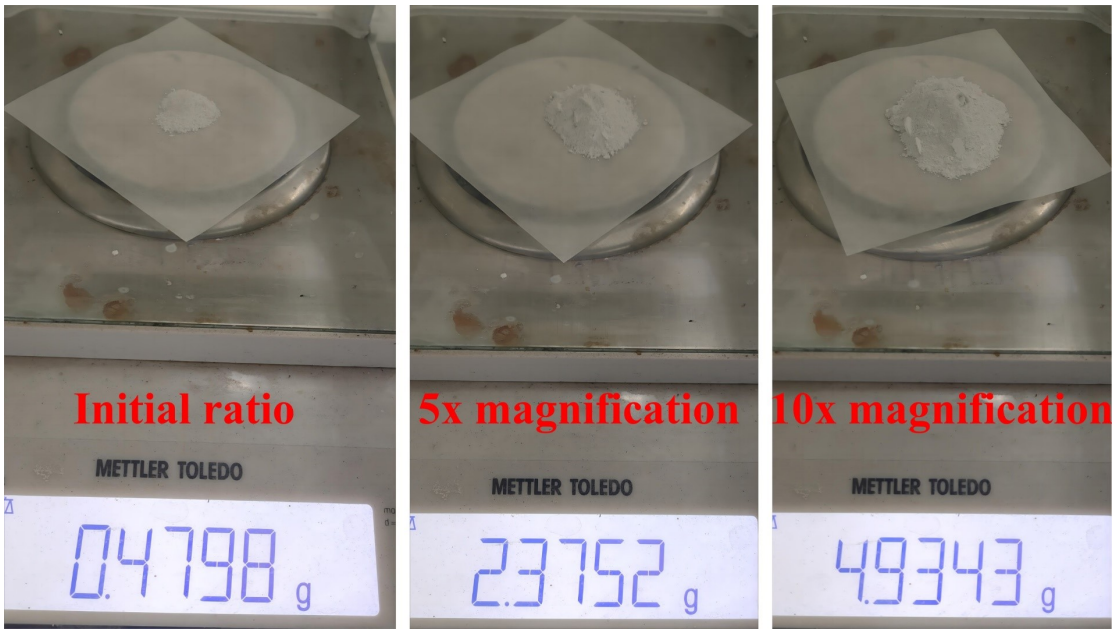

Fig. S14. Weighed digital photo of 1B/1M obtained by expanding precursors.

Reference

1 Y. Chen, X. Tang, J. Zhong, J. Li, M. Li and T. Zhang, Fabrication of tunable oxygen vacancies on BiOCl modified by spiral carbon fiber for highly efficient photocatalytic detoxification of typical pollutants, *Appl. Surf. Sci.*, 2022, **578**, 152122.

2 H. Wang, B. Liao, T. Lu, Y. Ai and G. Liu, Enhanced visible-light photocatalytic degradation of tetracycline by a novel hollow BiOCl@CeO_2 heterostructured microspheres: Structural characterization and reaction mechanism, *J. Hazard. Mater.*, 2020, **385**, 121552.

3 C. Tian, S. Luo, J. She, Y. Qing, N. Yan, Y. Wu and Z. Liu, Cellulose nanofibrils enable flower-like BiOCl for high-performance photocatalysis under visible-light irradiation, *Appl. Surf. Sci.*, 2019, **464**, 606-615.

4 Y. Wang, S. Zhang, Y. Yan, H. Ren, J. Chen, L. Liu and X. Wu, Multi-anions-coupled electronic states in Cl^--doped BiOBr induce highly efficient decomposition of tetracycline hydrochloride, *Mater. Res. Bull.*, 2023, **158**, 112045.

5 S. Li, M. Cai, C. Wang, Y. Liu, N. Li, P. Zhang and X. Li, Rationally designed Ta_3N_5/BiOCl S-scheme heterojunction with oxygen vacancies for elimination of tetracycline antibiotic and Cr(VI): Performance, toxicity evaluation and mechanism insight, *J. Mater. Sci. Technol.*, 2022, **123**, 177-190.

6 L. Yang, J. Wang, Y. Zhang, B. Zhou, P. Tan and J. Pan, Construction of S-scheme BiOCl/CdS composite for enhanced photocatalytic degradation of antibiotic, *J. Mater. Sci. Mater. Electron.*, 2022, **33**, 13303-13315.

7 Y. Cui, J. Zheng, Z. Zhu, C. Hu and B. Liu, Preparation and application of Bi_4O_7/Cu-BiOCl heterojunction photocatalyst for photocatalytic degradation of tetracycline under visible light, *J.*

Mol. Struct., 2023, **1274**, 134486.

8 S. Bao, H. Liang, C. Li and J. Bai, A heterostructure BiOCl nanosheets/TiO_2 hollow-tubes composite for visible light-driven efficient photodegradation antibiotic, *J. Photochem. Photobiol. A*, 2020, **397**, 112590.

9 J. Wu, X. Fang, H. Dong, L. Lian, N. Ma and W. Dai, Bimetallic silver/bismuth-MOFs derived strategy for Ag/AgCl/BiOCl composite with extraordinary visible light-driven photocatalytic activity towards tetracycline, *J. Alloys Compd.*, 2021, **877**, 160262.

10 J. Dang, J. Guo, L. Wang, F. Guo, W. Shi, Y. Li and W. Guan, Construction of Z-scheme Fe_3O_4/BiOCl/BiOI heterojunction with superior recyclability for improved photocatalytic activity towards tetracycline degradation, *J. Alloys Compd.*, 2022, **893**, 162251.